ROYAL SOCIETY OF CHEMISTRY

PAPER

Check for updates

Protective buffer layer engineering for sputter-resistant transparent perovskite solar cells with improved transmission and efficiency

Abhijit Singha,†[a] Ananta Paul,†[b] Subir Manna,[c] Chinmaya Kumar Sahoo,[d] Vishnu Kumar,[c] Anil Kottantharayil,[e] Sudhanshu Mallick,[b] K. R. Balasubramaniam [iD] *[a] and Dinesh Kabra [iD] *[c]

The identification of an optimal sputter buffer layer with higher transmission and conductivity remains a critical challenge in the fabrication of transparent perovskite solar cells (T-PSCs). It plays a vital role in protecting the underlying layers during highly energetic radio frequency (RF) magnetron sputtering, a process known to induce surface damage, while facilitating excellent light transmission. This study explores five metal oxides (MOs) – Y_2O_3, SnO_2, WO_3, MoO_3, and Pr_6O_{11} – as potential sputtered buffer layers for the fabrication of efficient T-PSCs applicable for both substrate and superstrate configurations in tandem solar cells. The d-block metal oxides exhibited the highest optical average transmission (T_{av}) values of ~86% and ~88% across the visible and near-infrared (NIR) ranges under substrate and superstrate illumination conditions, respectively. Moreover, WO_3 facilitates an improved defect-free electronic coupling at the spiro-MeOTAD and IZO interface. As a result, the champion T-PSCs having E_g ~1.6 eV and an active area of 17.5 mm^2 achieved the highest power conversion efficiency (PCE) of 19% with an optimal buffer thickness, which effectively balances protection and low contact resistance. Concurrently, WO_3-based device shows an excellent transmission of ~42% in the wavelength range of 300–1200 nm and ~77% in the NIR range (800–1200 nm), which will be suitable for tandem applications. Additionally, the average transmission of ~26% and ~11% in the wavelength range of 300–900 nm and 390–780 nm, respectively, will be applicable for building-integrated PV (BIPV) applications. By coupling with 23% efficient monocrystalline passivated emitter rear contact (PERC) Si solar cells, a combined efficiency of 26.71% is achieved in four-terminal (4T) tandem configurations. Stability tests showed that the champion devices retained 90% efficiency after ~90 days under inert conditions and 80% under harsh thermal and moisture exposure for ~45 days. These results highlight the critical role of the buffer layer in advancing T-PSCs, offering improved performance and stability for scalable photovoltaic technologies.

Broader context

This work presents a systematic investigation into the influence of orbital electron-engineered, sputter-protected buffer layers on the performance of transparent perovskite solar cells (T-PSCs) employing an n–i–p configuration. The functionality of these buffer layers is critically assessed across both substrate and superstrate configurations, which are pivotal for advancing high-efficiency four-terminal (4T) and two-terminal (2T) tandem solar cells. Through an in-depth analysis of the electronic interactions between the valence orbitals of metal oxide buffer layers and the hole transport layer (HTL), this study identifies optimal materials that simultaneously enhance optical transmission, minimize contact and series resistance, and improve the fill factor. These synergistic effects enable the realization of efficient and stable T-PSCs suitable for tandem integration. By elucidating the critical role of interfacial electronic coupling and material properties, this work not only demonstrates the practical potential of perovskite tandem architectures but also establishes a robust platform for future innovations in scalable, high-performance photovoltaic technologies. Such advancements are poised to accelerate the widespread adoption of next-generation solar energy solutions.

[a]Department of Energy Science and Engineering, Indian Institute of Technology Bombay, Mumbai, 400076, India. E-mail: bala.ramanathan@ese.iitb.ac.in

[b]Department of Metallurgical Engineering and Material Science, Indian Institute of Technology Bombay, Mumbai, 400076, India

[c]Department of Physics, Indian Institute of Technology Bombay, Powai, Mumbai 400076, India. E-mail: dkabra@iitb.ac.in

[d]Centre for Research in Nanotechnology and Science, Indian Institute of Technology Bombay, Powai, Mumbai 400076, India

[e]Department of Electrical Engineering, Indian Institute of Technology Bombay, Powai, Mumbai 400076, India

† These authors contributed equally to this work.

Introduction

Organic–inorganic lead halide hybrid perovskite solar cells (PSCs) have achieved remarkable advancements in power conversion efficiency (PCE), starting from 3.8% to 27.0% since their emergence in 2009.[1–4] This swift evolution in PCE has made them the fastest-evolving photovoltaic technology to date. Key attributes such as a high absorption coefficient, longer carrier diffusion lengths, simple solution processing, and easy bandgap tunability underscore their potential as sustainable energy sources.[5–9] The excellent band gap tunability further enables their applicability in multi-junction or tandem solar cell configurations. In tandem architectures, transparent perovskite top cells are integrated on top of narrow bandgap absorbers using either mechanically stacked four-terminal (4T) or mono-lithically integrated two-terminal (2T) configurations. Such arrangements are designed to synergistically enhance overall PCE.[10–13] Notably, current efforts focus on augmenting the efficiency of crystalline silicon (Si) solar cells through perovskite-based tandem configurations, leveraging their proven PCE performance.[13–15] Recent milestones, such as Longi's reported 34.6% efficiency in monolithic 2T Si/perovskite tandems with an active area of 1 cm^2, underscore their practical viability and potential as a benchmark for future developments.[16] Furthermore, Longi's achievement of 30.1% efficiency in commercial M6 silicon wafers, along with QCells' demonstration of 28.6% efficiency in M10 wafers, highlights the remarkable progress towards the practical application of perovskite-based tandem solar cells.[17,18] This introduction sets the stage for exploring the transformative role of perovskite materials in advancing photovoltaic technology, particularly in tandem configurations aimed at achieving higher efficiencies and sustainability in solar energy production.

Transparent electrodes (TEs) play a critical role in transparent perovskite solar cells (T-PSCs), ensuring efficient charge collection while allowing light transmission for tandem applications. The performance of T-PSCs is strongly influenced by TE properties, specifically low sheet resistance, high carrier mobility, and high optical transmittance.[19] Various materials have been explored, and carbon-based electrodes, such as CVD-deposited graphene, achieved 12.02% efficiency (You *et al.*) and 6.2% efficiency (Lang *et al.*), though they are limited by the conductivity-transparency trade-off.[20,21] Silver nanowires (Ag-NWs) have also shown promise. Guo *et al.* reported 8.49%, Yang *et al.* reported 10.64%, and Han *et al.* reported 7.3%, though achieving <20 Ω^{-1} with >80% transmittance remains a challenge.[22–24]

Thus, transparent conductive oxides (TCOs) have emerged as compelling candidates. However, conventional TCOs such as indium tin oxide (ITO) and fluorine-doped tin oxide (FTO) are extensively employed as bottom TEs, their application as top TEs is constrained by intrinsic limitations. FTO requires high-temperature processing, while ITO suffers from reduced NIR transmission.[25] Alternatives include hydrogenated indium oxide (IO:H, Fu *et al.*, 14.2% efficiency), zirconium-doped indium oxide (IZrO, Aydin *et al.*, 15.6% efficiency), and

indium zinc oxide (IZO, Shen *et al.*, 18.1% efficiency).[26–28] Aluminium-doped zinc oxide (AZO, Fu *et al.*, 16.1%) provides an indium-free option but has lower conductivity and long-term stability issues.[29] Dielectric–metal–dielectric (DMD) structures, such as MoO_x–Ag–MoO_x and SnO_x–Ag–SnO_x (Yang *et al.* and Zhao *et al.*, both 11.5% efficiency), offer improved stability, though balancing optical transparency and photovoltaic performance remains challenging.[30,31]

Metal oxide-based TEs can be deposited through a number of deposition techniques, including radio-frequency (RF) sputtering, solution-based sol–gel spin coating, pulsed laser deposition (PLD), thermal vapor transport, *etc.*[32–35] Among these methods, RF sputtering is particularly favoured due to its ability to enable high-quality, uniform, and scalable film deposition at room temperature, with precise control over film properties. In contrast, techniques such as sol–gel spin coating (Stojanoska *et al.*), thermal vapour transport (Karn *et al.*), and pulsed laser deposition (Ramamoorthy *et al.*) require high processing temperatures, limiting their use in PSCs.[33–35]

The high kinetic energy of sputtered particles can damage the underlying soft organic charge transport layers (CTLs) of T-PSCs, necessitating the use of a buffer or protective interlayer to mitigate this damage.[36,37] The selection of an appropriate buffer layer is therefore critical, not only for protecting CTLs but also for enhancing photovoltaic performance as an additional passivation layer at that interface. Additionally, achieving an optimal balance between the transparency and conductivity of TEs often requires higher sputtering power, which further increases the risk of damaging organic layers.[38,39] Consequently, the design of robust buffer layers is essential to reduce such damage and enable the reproducible fabrication of high-efficiency T-PSCs. Several studies have explored different buffer layer strategies for this purpose. Zhang *et al.* employed a combination of solution-processed ZnO nanoparticles and atomic layer deposition (ALD)-assisted ZnO as a buffer layer for ITO deposition.[40] Fu *et al.* and Warner *et al.* utilized IO:H transparent electrodes in conjunction with thermally evaporated MoO_3 buffer layers of tailored thickness in *n–i–p* PSC architectures.[26,41] Aydin *et al.* incorporated a ZnO nanoparticle and bathocuproine (BCP) combination as a buffer layer for IZrO deposition in *p–i–n* structured PSCs.[27] Werner *et al.* and Shen *et al.* also applied thermally evaporated MoO_3 as a sputter buffer layer for IZO deposition, while Fu *et al.* used ZnO nanoparticles for AZO deposition in *p–i–n* PSCs.[28,29,42] Kranz *et al.* adopted thermally evaporated MoO_3 as a sputter buffer layer in *n–i–p* devices.[43]

Therefore, transition metal oxides (MOs) have emerged as promising buffer layer materials especially in *n–i–p* transparent PSCs due to their wide bandgap and excellent optical transparency.[44,45] Their compatibility with simple and reproducible thermal evaporation techniques makes them a strong contender. Additionally, the straightforward integration of thermal evaporation into existing vacuum-based manufacturing lines makes it particularly attractive for large-area device fabrication. Furthermore, the method allows precise control over film thickness and uniformity, which is essential for maintaining device consistency in commercial production. However,

thermal evaporation of MOs is highly sensitive to ambient conditions, often resulting in non-stoichiometric films with oxygen vacancies.[46] Interestingly, these vacancies can be beneficial in n–i–p PSCs, as they introduce bandgap states that promote hole injection despite the n-type nature of the material.

Although MoO_3 has been widely employed as a sputter buffer layer in the development of T-PSCs, its integration often results in a reduced fill factor (FF) and decreased transparency of the bottom cell, thereby limiting the overall performance of tandem configurations.[47–49] Consequently, there remains a notable gap in research and understanding regarding suitable buffer materials for n–i–p architecture-based T-PSCs beyond conventional MoO_3.[49] To address this, alternative transition metal oxides such as tungsten oxide (WO_x) and niobium oxide (NbO_y), have been explored. Park *et al.* demonstrated that modifying WO_x with NbO_y improved the PSC fill factor from 70.4% to 78.8%, achieving a peak PCE of 18.9% with the absorber perovskite band edge at 800 nm and an active area of 7.07 mm^2.[49] Despite this FF enhancement, these materials exhibited lower open circuit voltage (V_{OC}) and transparency, with a maximum V_{OC} of 1.02 V and peak transmission of ~75% even after anti-reflection coating (ARC) insertion. Consequently, their 4T Si/perovskite tandem efficiency reached only 26% with an active area of 7.07 mm^2. Magliano *et al.* incorporated vanadium oxide (V_2O_x) as a sputter buffer layer, demonstrating improved optical transmittance and stability; however, the efficiency is slightly lower compared to conventional MoO_x.[50] These findings underscore the critical need for suitable buffer layer materials to enhance the performance of n–i–p architecture-based T-PSCs.

In this work, we conducted a systematic investigation to identify a suitable buffer layer for T-PSCs through comprehensive analyses of carrier lifetime, contact resistance, photoluminescence, and PV performance for deployment in both superstrate (2T) and substrate (4T) tandem configurations. Various transition metal oxides with distinct valence orbitals (s, p, d, and f) were employed to elucidate the electronic interactions between spiro-MeOTAD and the IZO layer. Our findings reveal that d-orbital-based metal oxides facilitate enhanced coupling and interfacial passivation at the HTL/TE interface. This leads to improved optical average transmission (T_{av} ~86% and ~88% in the wavelength range of 300–1200 nm under the substrate (4T) and superstrate (2T) illumination conditions, respectively), reduced contact resistivity (~0.17 Ω cm^2), and superior PCE. Among the investigated materials, all d-orbital-based metal oxides demonstrated higher PCE compared to others. Notably, WO_3, a d-orbital transition metal oxide, enabled the development of T-PSCs having a bandgap of ~1.6 eV and an active area of 17.5 mm^2 with an impressive efficiency of 19% and the highest average optical transmission of ~42% across the wavelength range of 300–1200 nm. Additionally, the champion T-PSC shows ~77% average transmission in the NIR range (800–1200 nm) and ~26% in the wavelength range of 300–900 nm, which confirms its superior suitability for tandem and building-integrated PV (BIPV) applications, respectively. The four-terminal tandem configuration of champion T-PSCs and monocrystalline passivated

emitter rear contact (PERC) Si solar cells resulted in 26.71% efficiency. Moreover, stability analyses are performed on the d-block metal oxide-based T-PSCs under various environmental conditions, including dark storage, continuous heating at 65 °C, and continuous illumination. The WO_3-based buffer layer demonstrated superior stability, attributed to the reduction of non-radiative recombination channels at the HTL/TE interface. This study provides a pathway for the development of efficient and stable n–i–p architecture-based perovskite tandem solar cells.

Results

The primary challenge in fabricating T-PSCs is the efficient deposition of top TEs while preserving their structural integrity, *i.e.*, without damaging the soft organic CTLs (*e.g.*, spiro-MeOTAD) and/or the perovskite photo-absorber. In this study, a custom-built RF magnetron sputtering physical vapour deposition (PVD) tool is employed to deposit indium zinc oxide (IZO) TEs. Sputtering inherently involves high-energy particle bombardment, which often damages spiro-MeOTAD and underlying perovskite layers, leading to defect formation and reduced device performance.[36,37] To mitigate these effects, a buffer layer is typically introduced to absorb the energy from the sputtered particles, thereby preserving the structural integrity of the adjacent layers. The key criteria of an efficient buffer layer are to facilitate smooth charge transport through tunnelling while ensuring high optical transparency. This work focuses on the fabrication of n–i–p architecture-based T-PSCs, utilizing a triple cation perovskite absorber material with the composition $Cs_{0.05}(FA_{0.83}MA_{0.17})_{0.95}Pb(I_{0.83}Br_{0.17})_3$, which has a bandgap ($E_g$) of ~1.6 eV.

Fig. 1(a) illustrates the device structure: glass/SnO_2/perovskite/spiro-MeOTAD/MOs. The cross-sectional field emission scanning electron microscopy (FESEM) image depicting all the complete layer structure of the T-PSCs, along with absorption analysis of the perovskite layer, is shown in Fig. S1. Our primary objective is to improve device performance and optical transmission beyond the perovskite band edge for applications in both 4T (substrate) and 2T (superstrate) tandem solar cell configurations. Hence, five different MOs [*e.g.*, yttrium oxide (Y_2O_3), tin oxide (SnO_2), tungsten oxide (WO_3), molybdenum oxide (MoO_3) and praseodymium oxide (Pr_6O_{11})] with diverse electronic configurations, encompassing elements from the s, p, d, and f blocks of the periodic table, are chosen as buffer layers for this study [Note: Y_2O_3 is classified under the s-block category owing to its analogous electronic configuration and the unavailability of corresponding s-block metal oxides.] This systematic study employs investigation of the optoelectronic properties of the MO layers, including parasitic absorption loss, transmission characteristics, contact resistance and the electronic interaction with the adjacent layers. This preliminary analysis ensures a deeper understanding of the material's behaviour with CTLs and TEs, laying a solid foundation for the subsequent fabrication process. All the MOs are deposited *via* the thermal evaporation method on a 20 × 20 mm^2 glass substrate to characterize the optical and electrical properties.
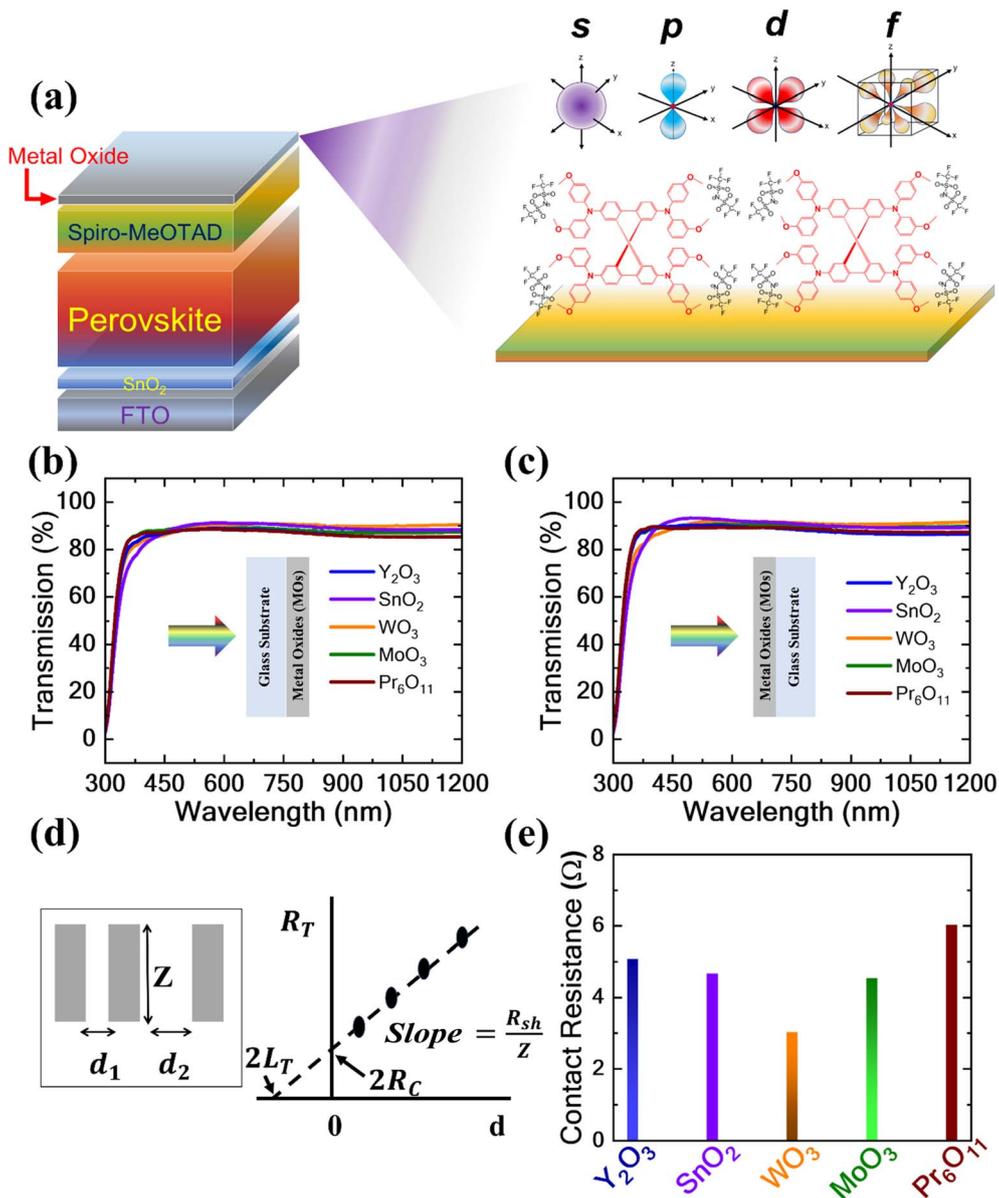
Fig. 1 Optoelectronic study of the s, p, d, and f valence electron-based metal oxides. (a) Device structure of the T-PSCs up to MO buffer layers (glass/SnO$_2$/perovskite/spiro-MeOTAD/MOs), transmission spectra of MOs under (b) bottom and (c) top side illumination respectively, (d) schematic representation of the transfer length method (TLM) setup, where R_c represents contact resistance, R_T represents total resistance, and L_t represents the transfer length and (e) variation of the contact resistance across different MOs at the spiro-MeOTAD/MO/IZO interface.

Fig. 1(b) shows the transmission spectrum of all the MOs (i.e., Y$_2$O$_3$, SnO$_2$, WO$_3$, MoO$_x$, and Pr$_6$O$_{11}$) in the range of 300–1200 nm when light is shining from the glass/MOs side, which is applicable for a 4T tandem configuration. The average transmission (T_{av}) of the MO films is 84.02% (Y$_2$O$_3$), 85.47% (SnO$_2$), 86.41% (WO$_3$), 85.41% (MoO$_3$), and 84.23% (Pr$_6$O$_{11}$), respectively, which is also shown in Fig. S2. Among all the MOs, the maximum T_{av} is observed for WO$_3$. The transmission spectrum for WO$_3$ is also higher in the NIR region than in the other MOs due to the lower parasitic absorption of WO$_3$. On the other hand, we also studied the transmission of the MOs when the light is shining from the MOs/glass side, which is applicable for a 2T tandem configuration, which is shown in Fig. 1(c).

The average transmission (T_{av}) for this case is as follows: 85.56% (Y$_2$O$_3$), 86.92% (SnO$_2$), 87.57% (WO$_3$), 87.32% (MoO$_3$), and 85.87% (Pr$_6$O$_{11}$). Here, also, WO$_3$ provides the highest T_{av}, among all the MOs (Fig. S2). One notable observation is that when light is incident from the MOs/glass side, the average transmittance (T_{av}) is higher compared to illumination from the bottom (glass/MOs) side. This is due to the lower reflection losses in the MO layers compared to the glass substrate, as the MO layers exhibit anti-reflective properties, which is shown in Fig. S3. Furthermore, the PV performance of the T-PSCs depends on the overall resistance of the device; thereby, the contact resistance (R_c) of the newly introduced interface HTL/ buffer layer/IZO needs to be characterized. The R_c value of the

five different MOs is estimated using the transfer length method (TLM). The TLM is commonly employed to assess contact resistance (R_c), sheet resistance (R_{sheet}), and specific contact resistivity (ρ_c).

Fig. 1(d) shows the schematic representation of the TLM experimental setup. The side view of the device architecture of TLM analysis is shown in Fig. S4. In this technique, co-planar and parallel electrodes of length L and width Z are placed at varying distances d on a conductive layer with uniform R_{sheet}, situated on an insulating substrate. The I–V characteristics are measured between consecutive electrode pairs across the entire TLM array. This method operates under the assumption of ohmic contact between the conductive layer and the electrodes. The total resistance (R_T) is calculated for each interelectrode distance and plotted against d. From this linear plot, as described in the equation[51]

$$R_T(d) = \frac{R_{sheet}}{Z}d + 2R_c \qquad (1)$$

$\frac{R_{sheet}}{Z}$ can be deduced from the slope and the R_c between the electrodes. R_{sheet} and R_c calculated from the TLM measurements are reliable only if the current is confined in one single layer. Thus, to determine R_c at the HTL/MOs/IZO interface, it is necessary to confine the lateral current in the MO layer. The contact resistance of the five different MO layers is shown in Fig. 1(e). The overall R_c follows the order: Pr_6O_{11} > Y_2O_3 > SnO_2 > MoO_3 > WO_3. The WO_3 film shows a minimum R_c value of ~3, which corresponds to a contact resistivity of ~0.17 Ω cm^2 (active area 0.058 cm^2).

The influence of the optical properties resulting from the incorporation of various MOs was investigated using photoluminescence (PL) imaging and intensity-dependent steady-state PL (SSPL) analysis. The experimental setup for PL
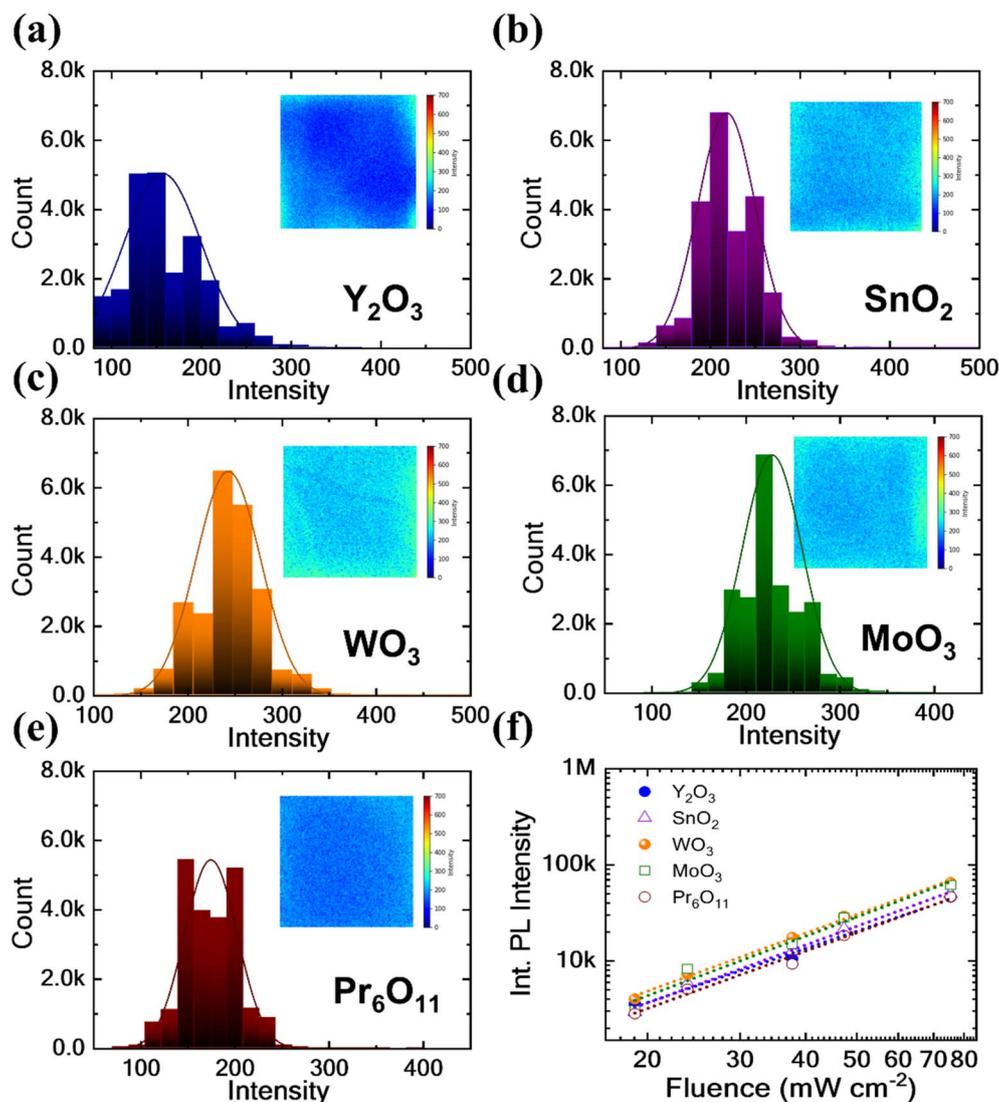

Fig. 2   Radiative intensity of the perovskite thin films with varying MO incorporations. (a)–(e) PL intensity distribution over a pixel area of 160 × 190 with different MO-based perovskite thin films, (inset: a PL image of the corresponding sample), and (f) linear fitting of the fluence-dependent PL analysis.

imaging is illustrated in Fig. S5. Fig. 2(a–e) show the distribution of PL intensity (PLI) over a pixel area of 160 × 190 and the corresponding PL images (inset) for perovskite films having different MOs, namely Y_2O_3, SnO_2, WO_3, MoO_3, and Pr_6O_{11}, respectively. Among these, films with MoO_3 and WO_3 buffer layers exhibited the highest PLI and showed uniform film coverage across the substrate, indicative of a well-deposited layer with minimal local inhomogeneity. In contrast, films incorporating Y_2O_3, SnO_2, and Pr_6O_{11} buffer layers demonstrated lower radiative intensity and inhomogeneity in their distribution. The overall intensity distribution followed the order: $WO_3 > MoO_3 > SnO_2 > Pr_6O_{11} > Y_2O_3$. Although MoO_3 is typically the preferred buffer layer in most $n–i–p$ architecture-based T-PSCs and also used for Si solar cells,[52] our experimental results reveal that WO_3 surpasses MoO_3 in terms of radiative intensity and transparency as a buffer layer for PV applications.

Fig. 2(f) presents the linear fit of the fluence-dependent SSPL intensity. The fitting results reveal a slope of 2 for perovskite films incorporating WO_3, MoO_3, and SnO_2 MO buffer layers. The Gaussian distribution of PL spectra at various fluence levels for perovskite thin films having different MOs is illustrated in Fig. S6. It is well established that a quadratic dependence of PLI on fluence (F), as indicated by the slope, suggests that the film is primarily governed by bimolecular recombination processes, as described in eqn (2).[53–55]

$$PLI \propto F^2 \qquad (2)$$

The bimolecular recombination process occurs when free electrons and holes recombine radiatively, which is indicative of high material quality. This process is highly desirable for achieving efficient optoelectronic applications and ensuring a higher quantum yield.[56] In contrast, the Y_2O_3 and Pr_6O_{11} metal oxide-based perovskite films exhibit slopes of 1.8 and 1.9, respectively. These values indicate the presence of non-radiative recombination processes, which could adversely affect the photovoltaic performance of the perovskite thin films. Additionally, the impact of carrier lifetime due to the incorporation of various MOs are investigated under both bottom (4T) and top (2T) illumination conditions using transient single-photon counting spectroscopy (TCSPC) analysis. The TCSPC decay profiles for the bottom and top illumination are presented in Fig. 3(a) and (b), respectively. Consistent with the PL analysis, the incorporation of d-block MOs resulted in higher carrier lifetimes, attributable to reduced non-radiative recombination pathways. Among the studied MOs, WO_3 exhibited the highest carrier lifetimes of ~110 ns and ~112 ns under bottom and top illumination conditions, respectively. The fitted carrier lifetimes follow the same trend observed in the PL analysis, ranking as $WO_3 > MoO_3 > SnO_2 > Pr_6O_{11} > Y_2O_3$. The fitted bi-exponential decay parameters of the TCSPC decay for all the MO-based perovskite films are tabulated in Table 1.

Parasitic absorption loss in the near-infrared (NIR) region is a significant challenge when aiming to achieve efficient tandem solar cells. The parasitic absorption largely depends on the thickness of the MOs; therefore, the quantitative optimization
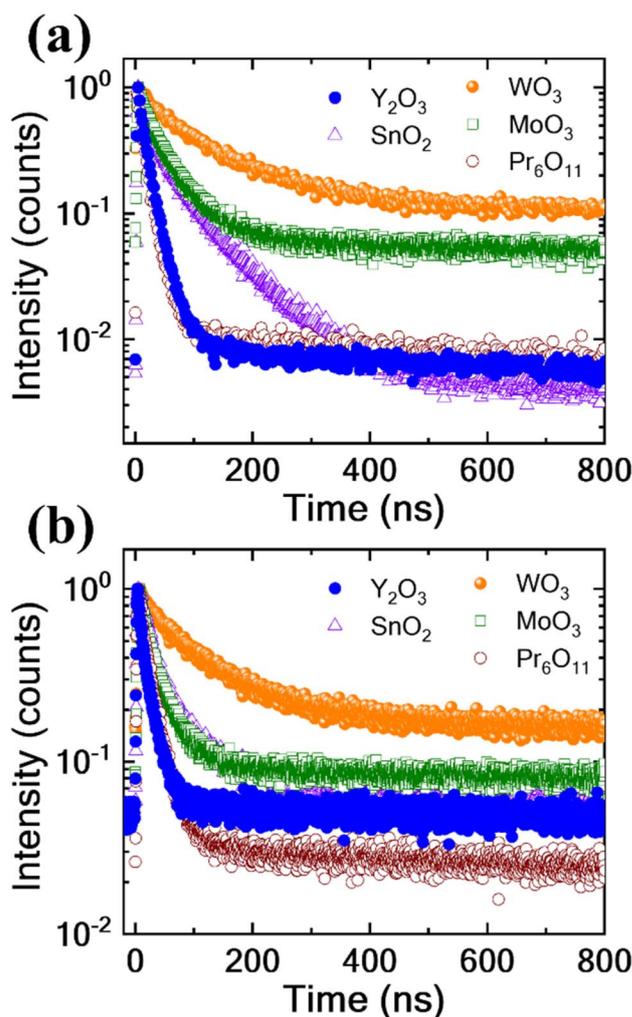

Fig. 3 Carrier lifetime analysis of the perovskite thin films with varying MO incorporation. TCSPC decay spectra of the perovskite thin films having different MO layers under (a) bottom and (b) top side illumination conditions.

Table 1 Bi-exponential fitting parameters of the TCSPC analysis of perovskite thin films having different MOs

MOs	Illumination side	A1	A2	τ_1	τ_2	Avg. τ (ns)
Y_2O_3	Bottom	0.77	0.47	9.4	21.46	16.5
	Top	0.5	0.6	5.74	19.75	17.1
SnO_2	Bottom	0.38	0.55	16.2	54.08	45.9
	Top	0.55	0.36	16.31	45.3	35.4
WO_3	Bottom	0.22	0.57	30.47	121.5	112
	Top	0.24	0.59	31.89	121.73	110.6
MoO_3	Bottom	0.49	0.45	15.54	70.68	60.2
	Top	0.7	0.19	24.15	81.28	51.3
Pr_6O_{11}	Bottom	0.75	0.01	13.05	194.63	34.5
	Top	0.06	0.97	62.57	17.09	25.6

of layer thickness is crucial. Thinner MOs have reduced parasitic absorption but are more susceptible to sputtering damage during fabrication. Conversely, thicker MOs can mitigate damage but lead to increased parasitic absorption followed by

additional parasitic resistance. To address these competing factors, we carefully varied the MO thickness that minimizes parasitic absorption, sputtering damage and resistive losses and struck a balance that enhances the overall performance and durability of the device. Moreover, the PV performance is analyzed by varying the thickness of each individual buffer layer, ranging from 5 to 15 nm. The results show that only the ~10 nm MO-based devices demonstrated better performance for all the cases, while the ~5 nm MO-based devices exhibited an 'S'-shaped J–V characteristic, which is denoted as the sputter damage effect (Fig. S7). For comprehensive analysis, T-PSCs are also fabricated without a buffer layer, exhibiting highly shunted J–V characteristics (Fig. S8 and Table S2). The origin of the 'S'-shaped J–V characteristics is due to the increased series resistance and poor charge transport at the interface, likely caused by the insufficient thickness of the ~5 nm MO buffer layer.[57] It is also noted that the 'S'-shaped characteristics are basically due to the double diode formation of a pseudo-Schottky diode with

the formation of a depletion layer at the interface.[57–60] However, Hiroyuki et al. reported that the TE sputter damage against spiro-OMeTAD increases barrier height and leads to a poor FF and thus J–V degradation ('S'-shaped or shunted J–V).[61] Hence, an adequate thickness of the buffer layer becomes essential to achieve the best performance from T-PSCs. Increasing the buffer layer thickness beyond 10 nm results in reduced device performance, primarily due to the higher series resistance of the buffer layer, which is evident from the loss in the FF and short-circuit current density (J_{SC}). Notably, the FF mainly decreases in devices with a ~15 nm buffer layer compared to those with a 10 nm layer (Table S1). Hence, the devices with a buffer layer thickness of ~10 nm show optimal performance, and we have fixed this for further analysis.

Fig. 4(a) presents the J–V characteristics of champion devices based on five different metal oxides (MOs) under 1-sun illumination (AM1.5 G, 100 mWcm^{-2}) measured in the reverse scan directions from the bottom side (glass/FTO). Among them, the
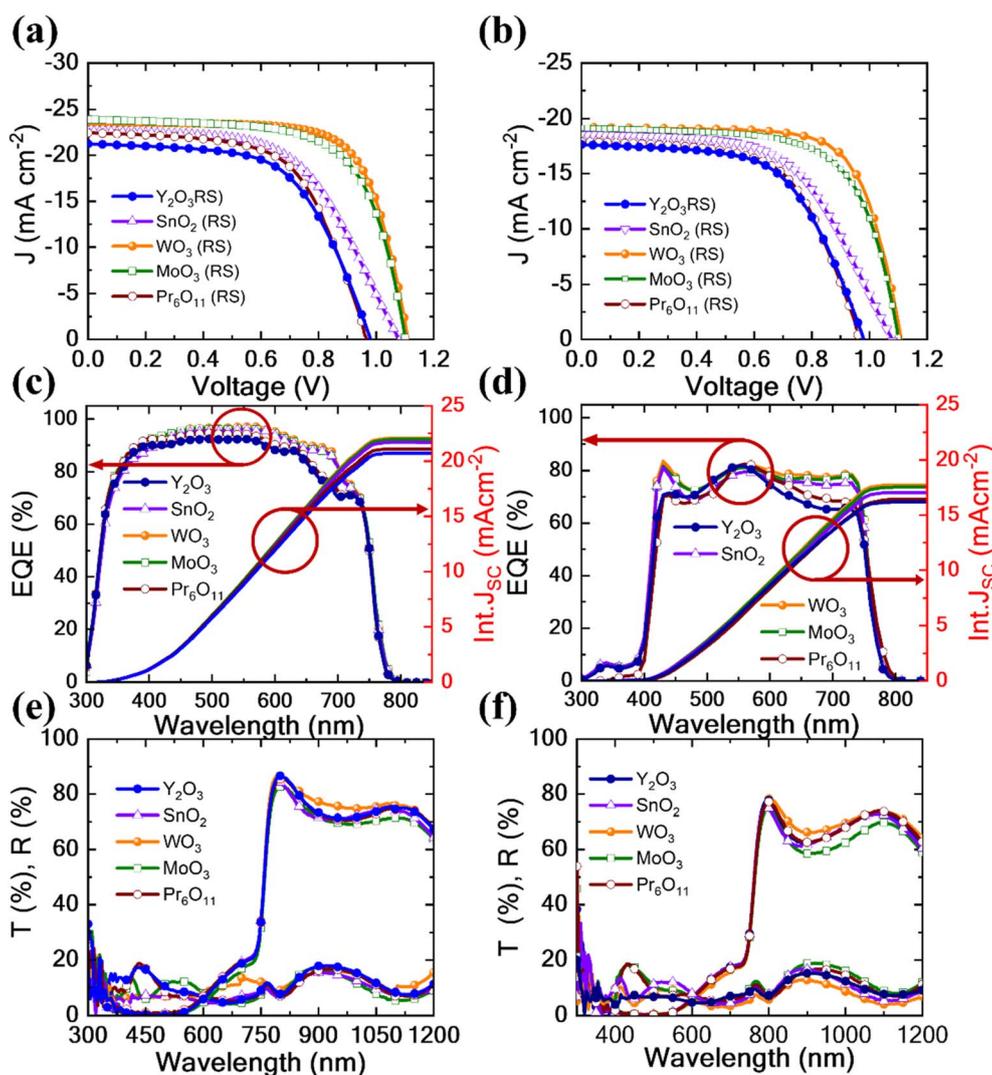

Fig. 4 Photovoltaic properties of the varying MO incorporating T-PSCs. (a) and (b). J–V characteristics under 1-sun conditions (AM 1.5 G; 100 mW cm^{-2}) (c) and (d) EQE with Int. J_{SC} and (e) and (f) transmission spectra of the T-PSCs under (a, c, and e) bottom and (b, d, and f) top side illumination conditions.

WO$_3$-based MO outperforms all others, achieving the highest PCE of 19% with $V_{OC} = 1.12$ V, $J_{SC} = 23.75$ mA cm^{-2}, and FF = 71.4%. In comparison, the Y$_2$O$_3$-based MO shows a PCE of 12.2% ($V_{OC} = 0.98$ V, $J_{SC} = 21.21$ mA cm^{-2}, and FF = 58.8%) and the SnO$_2$-based MO achieves a PCE of 13.9% ($V_{OC} = 1.08$ V, $J_{SC} = 22.62$ mA cm^{-2}, and FF = 56.7%). The MoO$_3$-based MO demonstrates a PCE of 17.4% ($V_{OC} = 1.1$ V, $J_{SC} = 23.64$ mA cm^{-2}, and FF = 66.8%), while the Pr$_6$O$_{11}$-based MO reaches a PCE of 13.2% ($V_{OC} = 0.96$ V, $J_{SC} = 22.45$ mA cm^{-2}, and FF = 61%). The J–V parameters clearly indicate that the d-block MO-based device exhibits superior performance, achieving the highest PCE among all the tested MOs. For baseline analysis, opaque PSCs incorporating a bi-layer Au/Ag counter electrode are also fabricated, as shown in Fig. S9. These devices achieved a maximum PCE of 20.0%, with a $V_{OC} = 1.13$ V, $J_{SC} = 23.78$ mA cm^{-2}, and FF = 74.4% respectively (Table S3). The performance of the opaque PSCs is consistent with that of previously reported champion devices, based on triple-cation mixed-halide perovskites with a bandgap of 1.6 eV.[3] These results confirm that the performance of the T-PSCs is not affected by fabrication artefacts. Additional statistical evaluations were performed on more than 30 devices (Fig. S10). Although the champion cell exhibits impressive PV performance, its efficiency is primarily constrained by a relatively low FF, which results from the higher sheet resistance of the top TE and the larger active area of the device. Table S4 presents a comparison between the current study and previously published literature since 2020 featuring the n–i–p architecture. It is evident that the PV performance and active area reported here are comparable to, or in some cases exceed, those in the referenced studies.

Fig. 4(b) presents the J–V characteristics of champion devices based on different MOs under 1-sun illumination (AM1.5 G, 100 mWcm^{-2}) measured in the reverse scan direction from the top side (IZO side). A similar trend in the photovoltaic performance is observed, i.e., the PSCs with d-block MOs perform well followed by p, f and s blocks, respectively. Among all the MOs, the PSC with WO$_3$ buffer layers exhibits the highest PCE under both substrate (4T) and superstrate (2T) illumination conditions. The PV parameters of all the champion devices with different MOs are tabulated in Table 2. The J–V characteristics and PV parameters of all the champion devices measured in the forward scan direction with different MOs under both bottom and top illumination are illustrated in Fig. S11(a) and (b),

respectively, and tabulated in Table S5. A significant improvement in the FF is observed for WO$_3$-incorporating PSCs, which can be attributed to reduced series resistance and enhanced shunt resistance, as detailed in Table S6. The higher shunt resistance can be further explained by the higher density of WO$_3$ (7.16 g cm^{-3}) thin films compared to MoO$_3$ (4.70 g cm^{-3}), leading to reduced sputter-induced damage.[62,63] Moreover, X-ray photoelectron spectroscopy (XPS) analysis is conducted on all the MOs, and the deconvoluted O 1s spectra revealed that WO$_3$ exhibits a higher concentration of oxygen vacancies compared to MoO$_3$ which is shown in Fig. S12 and Table S6. This increased vacancy density indicates that WO$_3$ possesses greater electrical conductivity, which in turn enhances the p-type characteristics of the spiro-MeOTAD HTL, thereby contributing to improved PV performance. Additionally, it is noteworthy that most metal oxides, except those from the d-block, require significantly higher power during thermal evaporation, which may be one of the contributing factors to the lower performance observed in PSCs incorporating these oxides.

The spectral response of all MO-based T-PSCs under bottom-side illumination is evaluated using external quantum efficiency (EQE) measurements, as depicted in Fig. 4(c). It is observed that the Y$_2$O$_3$ and Pr$_6$O$_{11}$-based devices exhibit a dip in the EQE spectrum within the wavelength range of 650–750 nm. In contrast, the other MOs maintain consistent EQE performance across this range without any noticeable photon loss. The integrated J_{SC} is further calculated from the EQE spectrum, with the WO$_3$-based device achieving the highest integrated J_{SC} of 22.10 mA cm^{-2} under front-side illumination, which corroborates well with the J–V analysis. This superior J_{SC} performance of WO$_3$ further emphasizes its advantage over the other metal oxides (Table 2). We understand that there is a slight mismatch between the current density obtained from EQE and J–V analysis. This is similar to the observations reported by Saliba et al., wherein there is a discrepancy in the Int. J_{SC} of 5–7%, where the J_{SC} obtained from the EQE measurements is lower compared to the J_{SC} calculated from the J–V analysis. This difference is attributed to the pre-bias measurement condition or edge effects in the device's active area.[64,65] Similarly, Fig. 4(d) presents the spectral response of MO-based T-PSCs under top-side illumination, assessed using EQE measurements. It is again observed that the Y$_2$O$_3$ and Pr$_6$O$_{11}$-based devices exhibit an unusual dip in the EQE spectrum

Table 2 J–V analysis parameters in reverse scan of the champion transparent PSCs of the five different MOs under AM1.5G illumination

Illumination side	Device	Scan	J_{SC} (mA cm^{-2})	V_{OC} (V)	FF (%)	PCE (%)	Int. J_{SC} (mA cm^{-2})
Bottom (glass/FTO)	Y$_2$O$_3$	RS	21.21	0.98	58.8	12.2	20.70
	SnO$_2$	RS	22.62	1.08	56.7	13.9	21.64
	WO$_3$	RS	23.75	1.12	71.4	19.0	22.10
	MoO$_3$	RS	23.64	1.10	66.8	17.4	21.96
	Pr$_6$O$_{11}$	RS	22.45	0.96	61.0	13.2	21.08
Top (IZO)	Y$_2$O$_3$	RS	17.61	0.98	58.8	10.1	16.18
	SnO$_2$	RS	18.55	1.08	56.9	11.4	17.05
	WO$_3$	RS	19.18	1.12	71.6	15.4	17.74
	MoO$_3$	RS	19.14	1.10	66.7	14.1	17.54
	Pr$_6$O$_{11}$	RS	17.91	0.96	61.0	10.5	16.44

within the 650–750 nm wavelength range. This behavior is primarily attributed to interfacial defects arising from poor electronic interaction between the MO, HTL and TE. Additionally, the EQE spectrum below 400 nm is not present under top-side illumination due to the absorption edge of the HTL and IZO (Fig. S13). The integrated J_{SC} is calculated from the EQE spectrum, with the WO_3-based device achieving the highest integrated J_{SC} of 17.47 mA cm^{-2} under top-side illumination, closely matching the J–V data (Table 2).

Fig. 4(e) shows the transmission and reflection spectra of T-PSCs with different MOs while illuminating light from the bottom side (4T). The average transmission (T_{av}) values are 40.94% for Y_2O_3, 40.52% for SnO_2, 42.01% for WO_3, 39.24% for MoO_3, and 41.02% for Pr_6O_{11}. In the NIR (800–1200 nm) region, the average transmission ($T_{avg-NIR}$) is 74.48% for Y_2O_3, 73.12% for SnO_2, 76.48% for WO_3, 71.65% for MoO_3, and 74.14% for Pr_6O_{11}. WO_3 stands out with the highest overall average transmission of 42% and the best NIR transmission of 76.48%, demonstrating superior transparency and outperforming all other MOs, particularly in the NIR region (Fig. S14). Fig. 4(f) shows the transmission and reflection spectra of devices with different MOs while illuminating light from the top side (2T). The average transmission (T_{avg}) values are 37.63% for Y_2O_3, 36.89% for SnO_2, 38.28% for WO_3, 35.79% for MoO_3, and 37.42% for Pr_6O_{11}. In the NIR region, the average transmission ($T_{avg-NIR}$) is 68.57% for Y_2O_3, 67.20% for SnO_2, 70.29% for WO_3, 64.39% for MoO_3, and 68.02% for Pr_6O_{11}. WO_3 stands out with the highest overall average transmission of 38.28% and the best

NIR transmission of 70.29%, demonstrating superior transparency and outperforming all other metal oxides, particularly in the NIR region (Fig. S14). It is observed from J–V characteristics that V_{OC} of the WO_3 buffer layer-based devices is slightly higher than that of the others, which further supports the PL analysis. PL imaging is conducted under open-circuit conditions and focuses on detecting photons generated during the radiative recombination of photogenerated charge carriers. This imaging technique enables the examination of the spatial distribution of charge carrier radiative recombination, allowing for a detailed analysis of non-radiative recombination and other resistive loss centers within the solar cells. The PLI analysis facilitates the evaluation of the radiative recombination current density (J_{rad}) using the above-stated mathematical relation, enabling the identification of the origin of voltage loss in the solar cell (Note 1). Reduced localized defects observed in PL imaging are associated with higher local voltages and brighter PL signals. Consequently, WO_3 exhibits the highest PLI, due to increased quasi-Fermi level splitting, thereby improving the open-circuit voltage (V_{OC}). This enhancement in V_{OC} follows the same trend as the PLI: $WO_3 > MoO_3 > SnO_2 > Pr_6O_{11} > Y_2O_3$. The long-term stability of the highest-performing d-block MO-based T-PSCs is investigated systematically.

Building on the enhanced transmission and efficiency of the champion T-PSCs, these devices are integrated with monocrystalline PERC Si solar cells in a 4T tandem configuration. Fig. S15 presents the EQE spectra of both standalone and perovskite-filtered Si solar cells. Based on the int. current
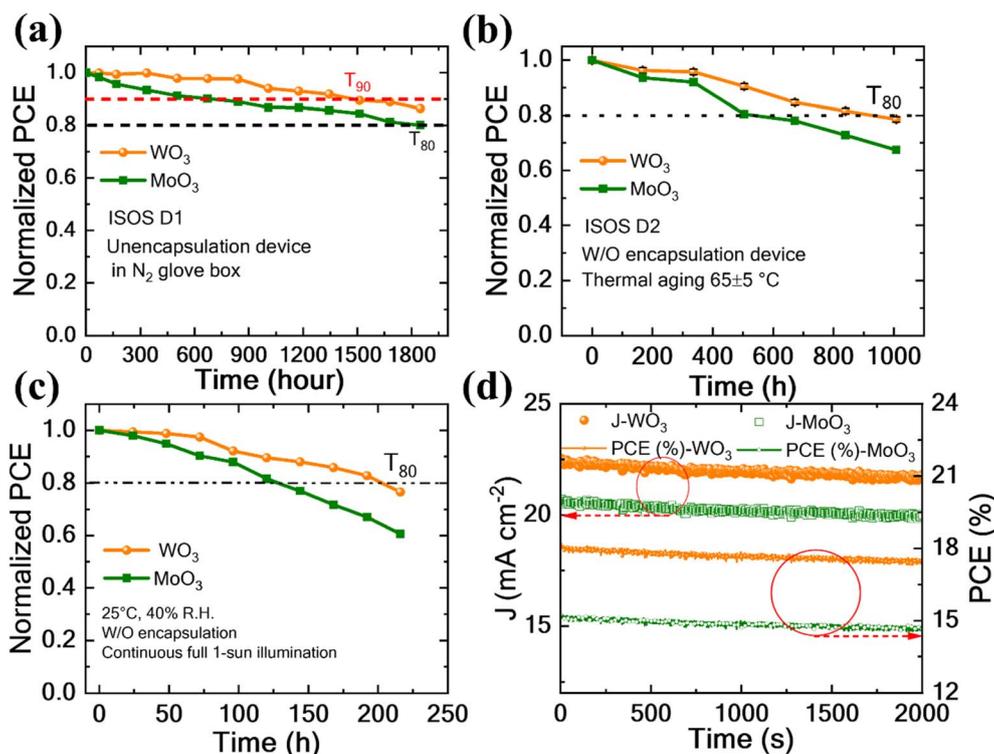

Fig. 5 Stability analysis of the d-block MO-based T-PSCs. (a) Shelf-life stability inside an N_2-filled glove box, (b) thermal stability test at continuous 65 ± 5 °C placed inside a muffle furnace, (c) light stability test under continuous 1-sun illumination (with an LED lamp), and (d) steady state PCE tracking at a constant voltage under 1-sun illumination of the unencapsulated T-PSCs.

density derived from the filtered EQE spectra of the Si solar cells, the performance of the 4T tandem configuration is calculated, yielding a filtered efficiency of 7.71% compared to the 23% efficiency of the standalone Si solar cells. The coupling of 19% efficient T-PSCs with the Si solar cells resulted in a combined efficiency of 26.71%, corresponding to an efficiency enhancement of over 16% for the Si solar cells. The detailed photovoltaic parameters are summarized in Table S8.

Fig. 5 shows the shelf or dark, thermal, light, and photo-stability of the T-PSCs. Shelf-stability testing involved storing devices inside an N_2-filled glovebox for more than 2000 h. The J–V analysis is conducted outside the glovebox during the shelf-stability test at a successive interval. Fig. 5(a) shows that after ageing in an N_2-filled glovebox, the WO_3-based T-PSCs retain ~90% of their initial efficiency up to ~1600 h. On the other hand, the MoO_3-based device shows T_{90} for ~600 h. The thermal stability test is conducted on unencapsulated solar cells with top IZO/MgF_2 contact placed in a muffle furnace at $65 \pm 5\,°$C at ambient humidity (ISOS D2). Fig. 5(b) shows the thermal stability studies of the d-block MO-based T-PSCs. The PCE of the WO_3-based device retains ~80% of its initial efficiency up to ~1000 h. And the MoO_3-based devices show similar thermal stability for ~700 h only. Light soaking tests for unencapsulated devices are conducted under continuous 1 sun (AM1.5G) illumination conditions with an LED lamp in a vacuum chamber at 25 °C, as depicted in Fig. 5(c). The PCE of the WO_3-based devices retains 80% of its initial efficiency up to ~200 h, whereas the MoO_3-based devices retain a similar efficiency only for ~125 h. These results suggest that T-PSCs with a WO_3 buffer layer are more stable compared to traditional MoO_3-based PSCs under various conditions. Furthermore, we have also performed maximum steady-state PCE tracking at constant potential, *i.e.*, tracking of photocurrent density and corresponding PCE under continuous illumination. The PCE obtained from MPPT shows a similar performance to that obtained from the J–V analysis for both cases, and a negligible drop in device performance is observed even after >40 minutes as shown in Fig. 5(d).

Discussion

The fabrication of T-PSCs presents a significant challenge in protecting sensitive organic layers, such as spiro-OMeTAD and the perovskite absorber, during RF magnetron sputtering. This process can lead to defect formation and eventual device degradation. As shown in Fig. S9, the champion opaque PSC exhibits a PCE of 20%. However, replacing the opaque metal electrode with an IZO top TE resulted in highly shunted J–V characteristics, as illustrated in Fig. S8. To address this, a thin (~5 nm) buffer layer was introduced at the HTL/IZO interface, which led to a slight improvement in PV performance; however, the J–V curve still exhibited an 'S'-shaped profile, indicating interfacial defects. Increasing the buffer layer thickness to ~10 nm resulted in further improvement, yielding enhanced J–V characteristics with minimal V_{OC} loss, as shown in Fig. S7. Nevertheless, a reduction in the FF was observed, suggesting that while thicker buffer layers improve device stability and reduce shunting, they may also introduce resistive losses. These

results highlight the critical role of an optimized buffer layer. Such a layer serves to absorb the kinetic energy of sputtered particles, thereby preserving the structural and electronic integrity of the underlying organic materials. Furthermore, it must maintain sufficient optical transparency and electrical conductivity to support efficient device operation. Thus, careful design and engineering of the buffer layer are essential for realizing high-performance, stable, T-PSCs.

In this study, five MOs, Y_2O_3, SnO_2, WO_3, MoO_3, and Pr_6O_{11}, having distinct valence electron configurations, are incorporated as potential sputtered buffer layers for the 4T and 2T tandem applications of T-PSCs. Evaluations of their optoelectronic properties revealed that WO_3 exhibited lower parasitic resistance and hence the highest optical transmission in the Vis-NIR range (average transmission of ~42% in the wavelength range of 300–1200 nm and ~77% in the NIR range (800–1200 nm)) and lower contact resistance (~3 Ω) making it the most effective buffer layer which is shown in Fig. 1. PL imaging and TCSPC analysis further indicated that devices with d-block MO (*e.g.*, WO_3 and MoO_3) buffers showed higher radiative intensity and longer carrier lifetime with uniform film coverage, correlating with improved performance as evinced in Fig. 2 and 3.

It is important to emphasize that, in the case of MOs, oxygen vacancies play a pivotal role in modulating their electronic properties, particularly their conductivity. In their stoichiometric form, MOs typically exhibit low electrical conductivity due to their inherently wide bandgap, which limits carrier concentration. To enhance conductivity, it is necessary to introduce non-stoichiometry, most effectively, by generating oxygen vacancies that act as donor states within the bandgap. XPS analysis clearly indicates that all studied MOs possess significant oxygen vacancy concentrations, ranging from approximately 22% to 45% as shown in Fig. S12 and Table S6. Among these, MoO_3 and WO_3 exhibit oxygen vacancy levels of 22.02% and 24.40%, respectively, which appear to provide an optimal balance for achieving enhanced conductivity while maintaining desirable optical properties as evinced in prior studies. In addition to the role of oxygen vacancies, the Fermi level position within the MOs critically influences their performance in PV devices. Specifically, at the MO/spiro-MeOTAD interface, it has been well established that a close energetic alignment, or a slightly deeper Fermi level relative to the HOMO of spiro-MeOTAD, facilitates efficient charge transfer.[66] This results in an energetically favourable flow of electrons from the HTL to the MO, thereby creating an excess of holes within the spiro-MeOTAD layer and enhancing its p-type character.[66,67] In this regard, MoO_3 and WO_3, with work functions of 6.6–6.9 eV and 5.0–5.8 eV, respectively, exhibit particularly favorable interactions with the 5.2 eV HOMO level of spiro-MeOTAD.[68–71] Notably, WO_3 demonstrates strong interfacial coupling with spiro-MeOTAD, leading to significant p-type doping effects that improve charge extraction and overall device performance. Consequently, we believe that there is no substantial modulation of the effective work function of the HTL, as only a negligible change in V_{OC} is observed. Instead, the results suggest the establishment of Fermi level pinning, which subsequently facilitates enhanced hole extraction. It is therefore evident that

there exists a strong correlation between the d-block electronic structure of the MOs with a precise Fermi level and their ability to interact effectively with both spiro-MeOTAD and IZO TEs. These synergistic interactions render MoO_3 and WO_3 particularly advantageous for T-PSCs.

Furthermore, T-PSCs are fabricated using all MOs, and the influence of buffer layer thickness on PV performance is examined. An optimal thickness of $\sim$10 nm is determined to yield the best performance, while thinner layers result in shunted J–V characteristics due to sputter damage and higher thickness leads to parasitic resistance loss. Devices based on WO_3 achieved the highest PCE of 19%, significantly outperforming those using the other oxides. The J–V characteristics and EQE measurements corroborated these results, demonstrating that WO_3 maintained superior performance than the other d-block MOs, $i.e.$, MoO_3, which is normally used in n–i–p architecture based T-PSCs across various tests as shown in Fig. 4. The primary improvement exhibited in the FF and the parasitic resistance of the device, which can be correlated with the higher density of WO_3 compared to MoO_3, leads to lower sputter damage. Long-term stability assessments are performed on higher efficiency d-block MO-based PSCs. The WO_3-based devices show a higher PCE retention rate under all the different storage conditions. It retained $\sim$90% of its initial efficiency after $\sim$90 days in an inert atmosphere and $\sim$80% after extensive thermal and moisture exposure for $\sim$45 days. Light soaking tests and MPPT analysis confirmed the stable performance under continuous illumination and operational bias, which is shown in Fig. 5. Overall, this study emphasizes the critical role of buffer layers in the fabrication of T-PSCs, with WO_3 demonstrating superior optical and electronic properties, which lead to enhanced device performance and stability.

Conclusion

Buffer layers are essential for mitigating damage to sensitive organic layers during RF magnetron sputtering, ensuring structural integrity and enhancing the optical and electrical properties of T-PSCs. T-PSCs incorporating d-block MOs, such as WO_3 and MoO_3, exhibited enhanced radiative intensity, longer carrier lifetimes, and uniform film coverage, attributed to the favourable electronic interactions between the d-block orbitals and spiro-MeOTAD/IZO TEs. Among the studied MOs, WO_3 emerged as the most effective buffer layer, demonstrating superior optical transmission, minimal parasitic absorption, and low contact resistance, which collectively contributed to the highest PCE of 19%. The optimized device exhibits an average optical average transmission of $\sim$26% in the 300–900 nm wavelength range and $\sim$11% within the visible spectrum (390–780 nm), indicating its potential suitability for BIPV applications. It is noteworthy that there remains scope for further enhancement of transmission by reducing the thickness of the absorber layer, thereby allowing for improved optimization between device efficiency and visible light transmittance. Additionally, an optimal buffer layer thickness of $\sim$10 nm was determined to effectively balance protection against sputter damage and minimize parasitic resistance, ensuring optimal

device performance. Consequently, a Si/perovskite 4T tandem solar cell with an efficiency of 26.71% is developed, achieving a performance enhancement of over 16%. Long-term stability assessments further validated the robustness of d-block WO_3 metal oxide-based devices, which retained $\sim$90% efficiency after $\sim$90 days under inert conditions and $\sim$80% under prolonged thermal and moisture stress for $\sim$45 days. These findings emphasize the pivotal role of WO_3 in advancing T-PSC technology, showcasing its ability to enhance both performance and durability and paving the way for its integration into tandem applications and scalable photovoltaic technologies.

Conflicts of interest

The authors declare that they have no conflict of interest.

Data availability

The data supporting the findings of this study are available from the corresponding author upon reasonable request.

Supplementary information is available. See DOI: **https://doi.org/10.1039/d5el00113g**.

Acknowledgements

References

1 M. A. Green, E. D. Dunlop, M. Yoshita, N. Kopidakis, K. Bothe, G. Siefer, D. Hinken, M. Rauer, J. Hohl-Ebinger and X. Hao, *Prog. Photovoltaics*, 2024, **32**, 425–441.

2 S. Bitton and N. Tessler, *J. Mater. Chem. C*, 2021, **9**, 1888–1894.

3 A. Singha, A. Paul, N. Gaur, H. S. Bilkhu, A. Arya, V. Bhalerao, S. Mallick, K. R. Balasubramaniam and D. Kabra, *Small*, 2025, **21**, 2502659.

4 NREL, *Best Research-Cell Efficiency Chart*, **https://www.nrel.gov/pv/cell-efficiency**, accessed 16 June 2025.

5 S. Singh, G. Banappanavar and D. Kabra, *ACS Energy Lett.*, 2020, **5**, 728–735.

6 A. Tara, A. Paul, A. Singha, S. Gohri, J. Madan, R. Pandey, P. Kumar, I. Hossain and S. Bhattarai, *J. Nanopart. Res.*, 2024, **26**, 278.

7 M. Degani, Q. An, M. Albaladejo-Siguan, Y. J. Hofstetter, C. Cho, F. Paulus, G. Grancini and Y. Vaynzof, *Sci. Adv.*, 2021, **7**, 7930.

8 J. T. W. Wang, Z. Wang, S. Pathak, W. Zhang, D. W. Dequilettes, F. Wisnivesky-Rocca-Rivarola, J. Huang, P. K. Nayak, J. B. Patel, H. A. Mohd Yusof, Y. Vaynzof, R. Zhu, I. Ramirez, J. Zhang, C. Ducati, C. Grovenor,

M. B. Johnston, D. S. Ginger, R. J. Nicholas and H. J. Snaith, *Energy Environ. Sci.*, 2016, **9**, 2892–2901.

9 Y. Vaynzof, D. Kabra, L. Zhao, P. K. H. Ho, A. T. S. Wee and R. H. Friend, *Appl. Phys. Lett.*, 2010, **97**, 156.

10 A. Paul, A. Singha, K. Hossain, S. Gupta, M. Misra, S. Mallick, A. H. Munshi and D. Kabra, *ACS Energy Lett.*, 2024, **9**, 3019–3026.

11 T. C.-J. Yang, T. Kang, M. Fitzsimmons, G. Vega, Y. Lu, L. Rosado, A. Jiménez-Solano, L. Pan, S. J. Zelewski, J. Ferrer Orri, Y.-H. Chiang, D. Guo, Z. Y. Ooi, Y. Han, W. Xu, B. Roose, C. Ducati, S. Carretero Palacios, M. Anaya and S. D. Stranks, *EES Sol.*, 2025, **1**, 41–55.

12 D. Chojniak, M. Steiner, S. K. Reichmuth, A. Schmid, G. Siefer, S. Hooper, D. Bushnell, D. Kirk, C. Case and S. W. Glunz, *EES Sol.*, 2025, **1**, 66–77.

13 E. Ugur, A. A. Said, P. Dally, S. Zhang, C. E. Petoukhoff, D. Rosas-Villalva, S. Zhumagali, B. K. Yildirim, A. Razzaq, S. Sarwade, A. Yazmaciyan, D. Baran, F. Laquai, C. Deger, I. Yavuz, T. G. Allen, E. Aydin and S. De Wolf, *Science*, 6708, **385**, 533–538.

14 F. Ji, G. Boschloo, F. Wang and F. Gao, *Sol. RRL*, 7, **6**, 2201112.

15 S. Mariotti, E. Köhnen, F. Scheler, K. Sveinbjörnsson, L. Zimmermann, M. Piot, F. Yang, B. Li, J. Warby, A. Musiienko, D. Menzel, F. Lang, S. Keßler, I. Levine, D. Mantione, A. Al-Ashouri, M. S. Härtel, K. Xu, A. Cruz, J. Kurpiers, P. Wagner, H. Köbler, J. Li, A. Magomedov, D. Mecerreyes, E. Unger, A. Abate, M. Stolterfoht, B. Stannowski, R. Schlatmann, L. Korte and S. Albrecht, *Science*, 2023, **381**, 63–69.

16 Longi, *34.6%! Record-breaker LONGi Once Again Sets a New World Efficiency for Silicon-perovskite Tandem Solar Cells*, 2024.

17 Longi, *LONGi announces the new world record efficiency of 30.1% for the commercial M6 size wafer-level silicon-perovskite tandem solar cells*, 2024.

18 P. Kelly, *Qcells reaches 28.6% efficiency on full-size tandem perovskite-silicon solar cell*, 2024.

19 Z. Wang, D. Lu, J. Jiang, W. Yan, Y. Gong, S. Wu, Y. Zhang, W. Huang and H. Xin, *ACS Appl. Energy Mater.*, 2020, **3**, 9742–9749.

20 P. You, Z. Liu, Q. Tai, S. Liu and F. Yan, *Adv. Mater.*, 2015, **27**, 3632–3638.

21 F. Lang, M. A. Gluba, S. Albrecht, J. Rappich, L. Korte, B. Rech and N. H. Nickel, *J. Phys. Chem. Lett.*, 2015, **6**, 2745–2750.

22 F. Guo, H. Azimi, Y. Hou, T. Przybilla, M. Hu, C. Bronnbauer, S. Langner, E. Spiecker, K. Forberich and C. J. Brabec, *Nanoscale*, 2015, **7**, 1642–1649.

23 K. Yang, F. Li, J. Zhang, C. P. Veeramalai and T. Guo, *Nanotechnology*, 2016, **27**(9), 095202.

24 K. Han, M. Xie, L. Zhang, L. Yan, J. Wei, G. Ji, Q. Luo, J. Lin, Y. Hao and C. Q. Ma, *Sol. Energy Mater. Sol. Cells*, 2018, **185**, 399–405.

25 K. Ellmer, *Nat. Photonics*, 2012, **6**, 809–817.

26 F. Fu, T. Feurer, T. Jäger, E. Avancini, B. Bissig, S. Yoon, S. Buecheler and A. N. Tiwari, *Nat. Commun.*, 2015, **6**, 8932.

27 E. Aydin, M. De Bastiani, X. Yang, M. Sajjad, F. Aljamaan, Y. Smirnov, M. N. Hedhili, W. Liu, T. G. Allen, L. Xu, E. Van Kerschaver, M. Morales-Masis, U. Schwingenschlögl and S. De Wolf, *Adv. Funct. Mater.*, 2019, **29**, 1901741.

28 H. Shen, T. Duong, J. Peng, D. Jacobs, N. Wu, J. Gong, Y. Wu, S. K. Karuturi, X. Fu, K. Weber, X. Xiao, T. P. White and K. Catchpole, *Energy Environ. Sci.*, 2018, **11**, 394–406.

29 F. Fu, T. Feurer, T. P. Weiss, S. Pisoni, E. Avancini, C. Andres, S. Buecheler and A. N. Tiwari, *Nat. Energy*, 2017, **2**, 16190.

30 Y. Yang Michael, Q. Chen, Y. T. Hsieh, T. Bin Song, N. De Marco, H. Zhou and Y. Yang, *ACS Nano*, 2015, **9**, 7714–7721.

31 J. Zhao, K. O. Brinkmann, T. Hu, N. Pourdavoud, T. Becker, T. Gahlmann, R. Heiderhoff, A. Polywka, P. Görrn, Y. Chen, B. Cheng and T. Riedl, *Adv. Energy Mater.*, 2017, **7**(14), 1602599.

32 E. Aydin, C. Altinkaya, Y. Smirnov, M. A. Yaqin, K. P. S. Zanoni, A. Paliwal, Y. Firdaus, T. G. Allen, T. D. Anthopoulos, H. J. Bolink, M. Morales-Masis and S. De Wolf, *Matter*, 2021, **4**(11), 3549–3584.

33 I. Stojanoska, M. Okorn, B. Kmet, H. Uršič, V. Gradišnik, D. Čakara, J. Kovač and D. Kuscer, *Heliyon*, 2023, **9**(9), e19744.

34 A. Karn, M. Kumar, V. N. Singh, B. R. Mehta, S. Aravindan and J. P. Singh, *Chem. Vap. Deposition*, 2012, **18**, 295–301.

35 K. Ramamoorthy, K. Kumar, R. Chandramohan, K. Sankaranarayanan, R. Saravanan, I. V. Kityk and P. Ramasamy, *Opt. Commun.*, 2006, **262**, 91–96.

36 E. Aydin, C. Altinkaya, Y. Smirnov, M. A. Yaqin, K. P. S. Zanoni, A. Paliwal, Y. Firdaus, T. G. Allen, T. D. Anthopoulos, H. J. Bolink, M. Morales-Masis and S. De Wolf, *Cell Press*, 2021, preprint, DOI: DOI: **10.1016/j.matt.2021.09.021**.

37 Q. Yang, W. Duan, A. Eberst, B. Klingebiel, Y. Wang, A. Kulkarni, A. Lambertz, K. Bittkau, Y. Zhang, S. Vitusevich, U. Rau, T. Kirchartz and K. Ding, *J. Mater. Chem. A*, 2024, **12**, 14816–14827.

38 J. Y. Hwang and S. Y. Lee, *Appl. Opt.*, 2024, **63**, 249.

39 G. T. Chavan, Y. Kim, M. Q. Khokhar, S. Q. Hussain, E. C. Cho, J. Yi, Z. Ahmad, P. Rosaiah and C. W. Jeon, *Nanomaterials*, 2023, **13**(7), 1226.

40 D. Zhang, M. Najafi, V. Zardetto, M. Dörenkämper, X. Zhou, S. Veenstra, L. J. Geerligs, T. Aernouts and R. Andriessen, *Sol. Energy Mater. Sol. Cells*, 2018, **188**, 1–5.

41 J. Werner, C. H. Weng, A. Walter, L. Fesquet, J. P. Seif, S. De Wolf, B. Niesen and C. Ballif, *J. Phys. Chem. Lett.*, 2016, 7, 161–166.

42 J. Werner, G. Dubuis, A. Walter, P. Löper, S. J. Moon, S. Nicolay, M. Morales-Masis, S. De Wolf, B. Niesen and C. Ballif, *Sol. Energy Mater. Sol. Cells*, 2015, **141**, 407–413.

43 L. Kranz, A. Abate, T. Feurer, F. Fu, E. Avancini, J. Löckinger, P. Reinhard, S. M. Zakeeruddin, M. Grätzel, S. Buecheler and A. N. Tiwari, *J. Phys. Chem. Lett.*, 2015, **6**, 2676–2681.

44 T. L. Chiu and Y. T. Chuang, *J. Phys. D Appl. Phys.*, 2015, **8**(7), 075101.

45 A. Paul, A. Singha, S. Koul, S. Nayak, N. Gaur, S. Mallick, B. Kavaipatti and D. Kabra, *ACS Appl. Mater. Interfaces*, 2024, **16**, 60258–60267.

46 M. C. Rao, K. Ravindranadh, A. Kasturi and M. S. Shekhawat, *Structural Stoichiometry and Phase Transitions of MoO₃ Thin Films for Solid State Microbatteries*, 2013, vol. 2.

47 Z. Wang, D. Lu, J. Jiang, W. Yan, Y. Gong, S. Wu, Y. Zhang, W. Huang and H. Xin, *ACS Appl. Energy Mater.*, 2020, **3**, 9742–9749.

48 A. Singha, A. Paul, S. Koul, V. Sharma, S. Mallick, K. R. Balasubramaniam and D. Kabra, *Sol. RRL*, 2023, **7**(12), 2300117.

49 H. H. Park, J. Kim, G. Kim, H. Jung, S. Kim, C. S. Moon, S. J. Lee, S. S. Shin, X. Hao, J. S. Yun, M. A. Green, A. W. Y. Ho-Baillie, N. J. Jeon, T. Y. Yang and J. Seo, *Small Methods*, 2020, **4**(5), 2000074.

50 E. Magliano, P. Mariani, A. Agresti, S. Pescetelli, F. Matteocci, B. Taheri, A. Cricenti, M. Luce and A. Di Carlo, *ACS Appl. Energy Mater.*, 2023, **6**, 10340–10353.

51 S. Zogbo, W. Favre, O. Bonino and M. E. Gueunier-Farret, *Sol. Energy Mater. Sol. Cells*, 2024, **265**, 112623.

52 M. Shahbazi, A. Taherkhani and J. Nasrollah Gavgani, *Mater. Today Commun.*, 2023, **35**, 106263.

53 J. Chen, C. Zhang, X. Liu, L. Peng, J. Lin and X. Chen, *Photonics Res.*, 2021, **9**, 151.

54 T. Kirchartz, J. A. Márquez, M. Stolterfoht and T. Unold, Wiley-VCH Verlag, 2020, preprint, DOI: DOI: **10.1002/aenm.201904134**.

55 J. M. Richter, M. Abdi-Jalebi, A. Sadhanala, M. Tabachnyk, J. P. H. Rivett, L. M. Pazos-Outón, K. C. Gödel, M. Price, F. Deschler and R. H. Friend, *Nat. Commun.*, 2016, **7**, 13941.

56 C. L. Davies, M. R. Filip, J. B. Patel, T. W. Crothers, C. Verdi, A. D. Wright, R. L. Milot, F. Giustino, M. B. Johnston and L. M. Herz, *Nat. Commun.*, 2018, **9**, 293.

57 A. Wagenpfahl, D. Rauh, M. Binder, C. Deibel and V. Dyakonov, *Phys. Rev. B:Condens. Matter Mater. Phys.*, 2010, **82**, 115306.

58 P. Löper, S. J. Moon, S. Martín De Nicolas, B. Niesen, M. Ledinsky, S. Nicolay, J. Bailat, J. H. Yum, S. De Wolf and C. Ballif, *Phys. Chem. Chem. Phys.*, 2015, **17**, 1619–1629.

59 S. H. Demtsu and J. R. Sites, *Thin Solid Films*, 2006, **510**, 320–324.

60 B. Kouskoussa, M. Morsli, K. Benchouk, G. Louarn, L. Cattin, A. Khelil and J. C. Bernède, *Phys. Status Solidi A*, 2009, **206**, 311–315.

61 H. Kanda, A. Uzum, A. K. Baranwal, T. A. N. Peiris, T. Umeyama, H. Imahori, H. Segawa, T. Miyasaka and S. Ito, *J. Phys. Chem. C*, 2016, **120**, 28441–28447.

62 Wikipedia, *Tungsten trioxide*, 2025.

63 Wikipedia, *Molybdenum trioxide*, 2025.

64 K. Hossain, A. Kulkarni, U. Bothra, B. Klingebiel, T. Kirchartz, M. Saliba and D. Kabra, *ACS Energy Lett.*, 2023, **8**(9), 3860–3867.

65 F. S. F. Morgenstern, D. Kabra, S. Massip, T. J. K. Brenner, P. E. Lyons, J. N. Coleman and R. H. Friend, *Appl. Phys. Lett.*, 2011, **99**, 183307.

66 R. Hock, T. Mayer and W. Jaegermann, *J. Phys. Chem. C*, 2012, **116**, 18146–18154.

67 J. Meyer, S. Hamwi, M. Kröger, W. Kowalsky, T. Riedl and A. Kahn, *Adv. Mater.*, 2012, **24**(40), 5408–5427.

68 Y. Guo and J. Robertson, *Appl. Phys. Lett.*, 2014, **105**, 222110.

69 M. T. Greiner, L. Chai, M. G. Helander, W. M. Tang and Z. H. Lu, *Adv. Funct. Mater.*, 2013, **23**, 215–226.

70 G. Halek, I. D. Baikie, H. Teterycz, P. Halek, P. Suchorska-Woźniak and K. Wiśniewski, *Sens. Actuators, B*, 2013, **187**, 379–385.

71 F. Sanchez, L. Marot, A. Dmitriev, R. Antunes, R. Steiner and E. Meyer, *J. Alloys Compd.*, 2023, **968**, 171888.